Retention and multiphase transformation of selenium oxyanions during the formation of magnetite via ferrous hydroxide and green rust

Börsig, N.; Scheinost, A. C.; Shaw, S.; Schild, D.; Neumann, T.;

Originally published:

July 2018

Dalton Transactions 47(2018)32, 11002-11015

DOI: https://doi.org/10.1039/C8DT01799A

Retention and multiphase transformation of selenium oxyanions during the formation of magnetite via ferrous hydroxide and green rust

Nicolas Börsig [a,*], Andreas C. Scheinost [b,c], Samuel Shaw [d], Dieter Schild [e], Thomas Neumann [a]

[a] Karlsruhe Institute of Technology (KIT), Institute of Applied Geosciences, Adenauerring 20b, 76131 Karlsruhe, Germany

[b] Helmholtz-Zentrum Dresden-Rossendorf (HZDR), Institute of Resource Ecology, Bautzner Landstraße 400, 01328 Dresden, Germany

[c] The Rossendorf Beamline (ROBL) at ESRF, 38043 Grenoble, France

[d] The University of Manchester, School of Earth, Atmospheric and Environmental Sciences, Manchester, M13 9PL, United Kingdom

[e] Karlsruhe Institute of Technology (KIT), Institute for Nuclear Waste Disposal,
Hermann-von-Helmholtz-Platz 1, 76344 Eggenstein-Leopoldshafen, Germany

* Corresponding author: Tel.: +49 721 608-44878; nicolas.boersig@kit.edu (N. Börsig)

Keywords: selenite, selenate, selenide, iron oxide, reduction, oxidation, precipitation, immobilization, XPS, XAS, EXAFS

Abstract

Environmental and health hazards of the trace element Se are mainly related to the presence of highly mobile Se oxyanion species (oxidation states +4 and +6). In this study, we investigate the immobilization of dissolved Se oxyanions during the formation process of magnetite by the progressive oxidation of an alkaline, anoxic Fe^{2+} system (pH 9.2). Up to initial concentrations of $c(Se)_0 = 10^{-3}$ mol/L (m/V ratio = 3.4 g/L), logRd values of xxxx demonstrate a strong retention of Se oxyanions during this mineral formation process. This Se immobilization is due to the reduction of Se(IV) or Se(VI), resulting in the precipitation of sparingly soluble Se compounds. By XRD analysis, these Se compounds were identified as crystalline elemental Se(0) that occurred in all coprecipitation products after the completed magnetite formation. The time-resolved analysis of the Se retention during the magnetite formation and detailed spectroscopic analyses (XPS, XAS) of the involved solid phases showed that the reduction takes place under the anoxic conditions in the early phase of the coprecipitation process by the interaction with iron(II) hydroxide and green rust. Both minerals represent the primary Fe(II)-containing precipitation products in the aquatic Fe^{2+} system and the precursor phases of the later formed magnetite. Spectroscopic and electron microscopic analysis prove that this early Se interaction leads to the formation of a nanoparticulate iron selenide phase [FeSe], which is oxidized and transformed into trigonal gray elemental Se during the progressive oxidation of the system. Regarding the retention behavior of Se, it is irrelevant whether the oxidation of the

meta-stable iron oxide phases leads to the formation of magnetite only or also to other iron oxide phases like goethite. This reductive precipitation of Se induced by an interaction with metastable Fe(II)-containing iron oxide minerals should affect the mobility of Se oxyanions in contaminated environments, including the behavior of ^{79}Se in the near-field of HLW repositories.

1 Introduction

The trace element selenium (Se) is of special concern because of the extremely fine line between its opposing properties: At low concentrations, it is an essential nutrient for many organisms, at slightly higher quantities, however, it becomes a toxic contaminant (Lenz and Lens, 2009). In addition, Se occurs in high-level nuclear waste (HLW) in the form of the long-lived, harmful radionuclide ^{79}Se, which may play a crucial role for the long-term safety assessments of deep geological repositories (De Cannière et al., 2010; Jörg et al., 2010).

In nature, Se occurs in five different oxidation states (-II, -I, 0, IV, VI). Of particular relevance are the two higher oxidations states, where Se forms the oxyanions selenite [Se(IV)] and selenate [Se(VI)]. In aquatic systems, both Se oxyanions occur in the form of well soluble species, which are generally highly mobile due to their limited interaction with geological materials (Grambow, 2008; Fernández-Martínez and Charlet, 2009). By contrast, Se species of the oxidation states Se(-II), Se(-I) and Se(0) are characterized by forming sparingly soluble compounds like metal selenides or elemental Se (Séby et al., 2001). The oxidation state is therefore the key factor determining the biochemical behavior of Se, since parameters such as solubility, mobility, bioavailability and toxicity mainly depend on the occurrence of dissolved Se species (Dhillon and Dhillon, 2003; Winkel et al., 2015; Nothstein et al., 2016). For this reason, environmental health and safety hazards of Se are primarily associated with the presence or absence of Se oxyanions.

Regarding the oxidation state of Se in HLW, recent research has demonstrated that Se occurs as Se(-II) in spent nuclear fuel (Curti et al., 2014; Curti et al., 2015). The formation of mobile Se species is therefore rather unlikely given the predicted reducing conditions of most HLW repositories. The expected predominant Se oxidation state in vitrified HLW arising from nuclear fuel reprocessing plants, however, is Se(IV) in the form of selenite groups (Bingham et al., 2011). Moreover, it cannot be fully excluded that oxidation processes induced by long-term irradiation could also lead to a transformation to Se(VI) or selenate, respectively (Bingham et al., 2011). The oxidation state of Se and the associated dominant Se species in HLW is therefore dependent on the waste form.

The iron oxide magnetite [Fe_3O_4] is widespread in nature and a common mineral in sediments and soils. Furthermore, magnetite is the most likely corrosion product of the steel canisters (technical barrier) under the expected alkaline, anoxic conditions in the near-field of a HLW repository (Smailos et al., 1992; Miller et al., 2000; Wersin et al., 2003; Smart et al., 2008). The corrosion of elemental iron to magnetite is, however, not a single reaction, but involves an intermediate stage, which is associated with the presence of precursor phases such as iron(II) hydroxide or green rust (Cornell and Schwertmann, 2003). Due to the relevance of magnetite and its precursors for various environments, their influence on the behavior of dissolved Se oxyanions has been investigated in previous studies. It was found that mineral phases that contained a reduced iron species are basically able to reduce Se oxyanions under anoxic conditions. Besides magnetite (Scheinost and Charlet, 2008), this includes the minerals iron(II) hydroxide (Murphy, 1988; Zingaro et al., 1997), green rust (Myneni et al., 1997; Johnson and Bullen, 2003; Scheidegger et al., 2003) as well as elemental iron (Olegario et al., 2010; Yoon et al., 2011; Liang et al., 2013), iron(II) sulfides (Bruggeman et al., 2005; Scheinost et al., 2008) or Fe^{2+} adsorbed on clay minerals (Charlet et al., 2007). Since reduction of Se oxyanions causes the formation of sparely soluble compounds, this interaction generally result in the immobilization of Se. These Se compounds are either elemental Se or iron selenides, whereby the nature of the products varies depending on the involved iron phases, the hydrochemical conditions, and the reduction kinetics. Especially the latter seems to be the main cause why the majority of the above-mentioned studies identified elemental Se (Murphy, 1988; Myneni et al., 1997; Zingaro et al., 1997; Scheidegger et al., 2003; Bruggeman et al., 2005; Charlet et al., 2007; Chen et al., 2009) whereas only a few studies proved the occurrence of iron selenides (Scheinost et al., 2008; Scheinost and Charlet, 2008; Olegario et al., 2010). This can be attributed to the fact that a reduction to Se(-II) and formation of iron selenides is limited to a rapid reduction of Se oxyanions (Scheinost et al., 2008).

However, retention of Se oxyanions during the magnetite formation process has never been investigated in detail, although it is probable that both also interact at this stage. This applies, for instance, to the formation of magnetite due to the corrosion of elemental iron, which represents an important process in the above-mentioned surroundings of geological repositories. Another example is the formation of magnetite caused by biologically or abiotically induced transformation of instable iron minerals in natural environments like sediments or soils (Kämpf et al., 2011; Blume et al., 2016). Such mineral formation processes may affect the immobilization of Se oxyanions, which has been demonstrated for the formation of hematite via ferrihydrite (Börsig et al., 2017).

In this study, we examined the interaction processes that lead to an immobilization of Se(IV) or Se(VI) during the formation and growth of magnetite or its precursor phases. Aim of this work was to identify and to characterize the Se retention mechanisms and to assess retention capacity and stability. To achieve this, we performed coprecipitation experiments with magnetite and Se oxyanions at alkaline pH, which is especially relevant for the near-field of HLW repositories. Furthermore, another key aspect was to investigate in which way a change of the redox conditions affects the Se retention. For this reason, the redox conditions were changed from initial anoxic to later oxic conditions during the experiments. With the help of hydrochemical data and a detailed analysis of the precipitation products by spectroscopic and electron microscopic methods, we were able to prove that two main redox processes were involved in the Se immobilization.

2 Materials and Methods

2.1 Synthesis of magnetite

Magnetite (Mt) was synthesized in the laboratory by using a modified method of Schwertmann and Cornell (2000). This method was originally designed for the preparation of goethite (Gt) and based on the progressive oxidation of an anoxic aquatic Fe^{2+} system. By increasing the solution pH from neutral to alkaline conditions, it was possible to inhibit the formation of goethite and to produce pure magnetite. One advantage of this method is that the preparation of magnetite by oxidizing an initially aquatic Fe^{2+} system is more suitable to simulate the formation of magnetite in nature than a preparation based on the mixing of Fe^{2+} and Fe^{3+} solutions. For the synthesis of magnetite 5 g of $FeCl_2 \cdot 4\ H_2O$ were dissolved in 500 ml N_2-degassed Milli-Q water (~pH 3.5). After the addition of 55 ml 1 M KOH and the immediate precipitation of a bluish green compound (~pH 8), the suspension was titrated and buffered with 25 ml of 1 M $NaHCO_3$ solution, which led to a pH value of ~8.5. All solutions were made of analytically pure grade chemicals and de-ionized, N_2-degassed Milli-Q water (18.2 $M\Omega cm^{-1}$). Continuous stirring during and after the mixing resulted in a progressive oxidation of the anoxic Fe^{2+} system by atmospheric oxygen. Within the total reaction time of 48 hours, this input of oxygen caused the transformation of the bluish green precipitate in a magnetic black mineral phase. In order to analyze the initially formed precipitation products, the synthesis process was terminated after 30 minutes and 3 hours, respectively. With about 2 g precipitated iron oxide forming, the mass to volume ratio (m/V) between magnetite and the aqueous solution was approx. 3.4 g/L in these batch experiments. At the end of the 48 hour reaction time, the black precipitates were decanted and centrifuged. While a sample of the solutions was taken for the analysis of the Fe concentration and pH, a part of the solids were washed three times with Milli-Q water to remove Cl^- and HCO_3^- impurities. The washed magnetite samples were then dried at 40°C. The remaining part of the solid sample was dried without prior washing with Milli-Q water in order to preserve the surface characteristics of the sample. After drying, the aggregated particles were ground with an agate mortar and stored until analysis. In case of the initial precipitation products (magnetite precursor), the samples were not washed or dried after the respective reaction time but were stored in their original synthesis solution. This was done to avoid further oxidation and crystallization processes after the terminated reaction with oxygen.

2.2 Coprecipitation experiments

The general procedure as well as the subsequent sample preparation of the coprecipitation experiments were almost identical to those of the magnetite synthesis described above. To investigate the behavior of Se(VI) or Se(VI) during the coprecipitation with magnetite, various volumes of Se stock solutions were added to the dissolved Fe^{2+} prior to the mineral precipitation. Se stock solutions were prepared by dissolving defined quantities of Na_2SeO_3 or $Na_2SeO_4 \cdot 10\,H_2O$ in N_2-degassed Milli-Q water to receive total Se(IV) or Se(VI) concentrations of 0.1 mol/L and 1.0 mol/L. Se stock solution was added to obtain initial Se concentrations of 10^{-4} - 10^{-2} mol/L after the mixing of all solutions (m/V ratio = 3.4 g/L). These relatively high Se concentrations were necessary to obtain sufficiently high Se concentrations in the solid samples for the subsequent solid state analyses. After the completed mineral formation, the residual Se concentration in solution was analyzed to calculate the amount of removed Se(IV) or Se(VI). The maximum reaction time of the coprecipitation studies was also 48 hours. For the time-resolved investigation of the Se(IV) and Se(VI) retention behavior, however, precipitates and solutions were collected and analyzed also after reaction times of 30 minutes and 3 hours.

2.3 Analytical techniques

The Se and Fe concentrations in the aqueous phase were determined by ICP-OES (Varian 715ES) or ICP-MS (X-Series 2; Thermo Fisher Scientific Inc.) depending on the solution concentrations. X-Ray Diffraction (XRD) was used for analysis of the purity and mineral composition of the synthesized solid materials and was performed on a Bruker D8 Advance X-ray diffractometer (Cu Kα). In order to calculate the specific surface areas (SSA) of magnetite and its precursor phase, BET measurements were performed using a Quantachrome Autosorb 1-MP. The total Se content of the solid phases was determined by polarized Energy Dispersive

X-ray Fluorescence Spectroscopy (pEDXRF) using an Epsilon 5 (PANalytical). Electron microscopy with energy dispersive X-ray spectroscopy was used to characterize the morphology, the particle size, and the detailed chemical composition of the solid phases. Images were recorded using a LEO 1530 (Zeiss Inc.) SEM with a NORAN System SIX (Thermo Electron Corp.) EDX-System or alternatively via a FEI Talos F200X analytical S/TEM equipped with an integrated ChemiSTEM EDX system with four windowless silicon drift detectors. To examine the Se oxidation state and to identify elemental composition of the surface area, X-ray Photoelectron Spectroscopy (XPS) measurements were performed using a PHI 5000 VersaProbe II (ULVAC-PHI Inc.). Detailed information about measurement parameters and sample preparation are described in the Supporting Information.

X-ray Absorption Spectroscopy (XAS) analysis was carried out on selected Se-bearing samples to identify the Se oxidation state as well as the nature of the molecular Se structure. Se K-edge X-ray Absorption Near-Edge Structure (XANES) and Extended X-ray Absorption Fine-Structure (EXAFS) spectra were collected at the Rossendorf Beamline (ROBL) at ESRF (Grenoble, France). Measurement parameters and sample preparation are described in detail in the Supporting Information. The XAS data reduction, including dead time correction of the fluorescence signal, energy calibration and the averaging of single scans were performed with the software package SixPack (Webb xxxx). Normalization, transformation from energy into k space, and subtraction of a spline background was performed with WinXAS using routine procedures (Ressler, 1998). The k^3-weighted EXAFS data were fit in R space with WinXAS using theoretical back-scattering amplitudes and phase shifts calculated with FEFF 8.2 (Ankudinov and Rehr, 1997). Statistical analysis of spectra was performed with the ITFA program package (Rossberg et al., 2003). Spectra of Se reference samples (Se(IV) solution as well as crystalline achavalite, ferroselite, and gray elemental Se) were taken from Scheinost and Charlet (2008).

3 Results and Discussion

3.1 Characterization of synthesized magnetite and its precursor phases

XRD patterns of synthesized magnetite after the total reaction of 48 h showed that pure magnetite [Fe_3O_4] was formed without any evidence of goethite contaminations. For the magnetite precursor phases (reaction time 30 min or 3 h), the XRD analysis revealed that these samples consist of a mixture of different mineral phases (SI Fig. A.1). The XRD patterns are dominated by a broad peak, which can be attributed to the presence of an amorphous or poorly crystalline mineral phase. In their description of the synthesis method, Schwertmann & Cornell

(2000) point out that the oxidation of the anoxic aquatic Fe^{2+} system takes place with the participation of iron(II) hydroxide phases. These phases are the immediate precipitation products after the first increase of the solution pH and also represent the unstable precursors of the subsequently forming (meta-) stable Fe (hydr)oxides. The occurrence of larger amounts of amorphous or poorly crystalline iron oxides in these samples is hence quite conceivable. Furthermore, one can identify peaks that are associated with the presence of small amounts of crystalline iron oxide phases such as magnetite and green rust, whereby the early magnetite formation is probably due to small quantities of dissolved oxygen in the synthesis solution. Besides that, small amounts of (hydrogen)carbonate salts occur in these unwashed samples (precipitated background electrolyte). BET measurements gave specific surface areas (SSA) of 32 m²/g for magnetite and 264 m²/g for its precursor phase after a reaction time of 30 min. The determined SSA of magnetite is consistent with published values in the literature. It is known that the SSA of synthesized magnetite can vary widely depending on its formation pathway and that, in particular, magnetite precipitation from solution can lead to very small particles with a SSA of up to 100 m²/g (Cornell and Schwertmann, 2003). The microscopic characterization (SEM) revealed that the pure magnetite consists of aggregated bulky particles with a size of about 50 nm (SI Fig. A.2). In case of the magnetite precursor phase, the high SSA of 264 m²/g is in good agreement with the XRD results suggesting a poorly crystalline mineral phase. However, one has to consider that the magnetite precursor might consist of several mineral phases and that the required sample drying before the BET analysis might has changed the characteristics of this sample type. By means of XPS analysis, it was possible to identify low amounts of Cl, K, and Na beside Fe and O in the near-surface region of an unwashed magnetite phase (SI Table A.1). This chemical composition is likely caused by adsorption of dissolved ionic species onto the magnetite surface. XPS analysis also enabled the determination of the Fe(II)/Fe_{total} ratio (here defined as $x_{Fe(II)}$) on the mineral surface. The used evaluation method is described in Huber et al. (2012) and is based on a comparison between the Fe 2p spectra of a sample and the Fe 2p spectra of references with known $x_{Fe(II)}$ values. Hematite and a freshly prepared magnetite were used as references, hence this method can only be applied to iron oxides but not to iron hydroxides or oxyhydroxides. With a determined $x_{Fe(II)}$ value of 0.14 the results indicate that the synthesized magnetite is partially oxidized to maghemite [γ-Fe_2O_3] at the end of synthesis process. Maghemite ($x_{Fe(II)} = 0$) is an oxidation product of magnetite ($x_{Fe(II)} = 0.33$) after the contact with atmospheric oxygen, and both minerals represent the end members of a solid solution series (Schwertmann and Cornell, 2000; Tang et al., 2003). However, since the XRD analysis showed no indication for the presence of maghemite, one can assume that mainly the surface region is affected by oxidation, but not the bulk phase. This assumption is supported by the fact that oxidation of magnetite in maghemite on the surface of magnetite particles can inhibit further oxidation processes (Rebodos and Vikesland, 2010).

3.2 Removal of Se(IV) and Se(VI) by coprecipitation

The analysis of the residual Se concentration allowed the determination of the Se(IV) or Se(VI) amount that was removed during the coprecipitation with magnetite. Figure 1 shows the quantities of Se associated with the solid phase as a function of the Se concentration at pH 9.2. Both data sets, the percentage of removed Se depending on the initial Se concentration (Fig. 1a) as well as the Se uptake depending on the Se equilibrium concentration (Fig. 1b), indicate that coprecipitation represents a highly efficient process to immobilize dissolved Se oxyanions. However, the results also demonstrate that the Se retention is affected by the speciation. For Se(VI), the uptake by coprecipitation decreases with higher initial Se concentrations and the Se(VI) sorption reaches an upper limit at ~1 mol/kg. By contrast, retention of Se(IV) is not influenced by higher initial Se amounts and even at concentrations of 10^{-2} mol/L all available Se is removed. The same applies to the total Se(IV) sorption, which rises to values of up to ~3 mol/kg and shows no indication of a sorption limit in the tested concentration range.

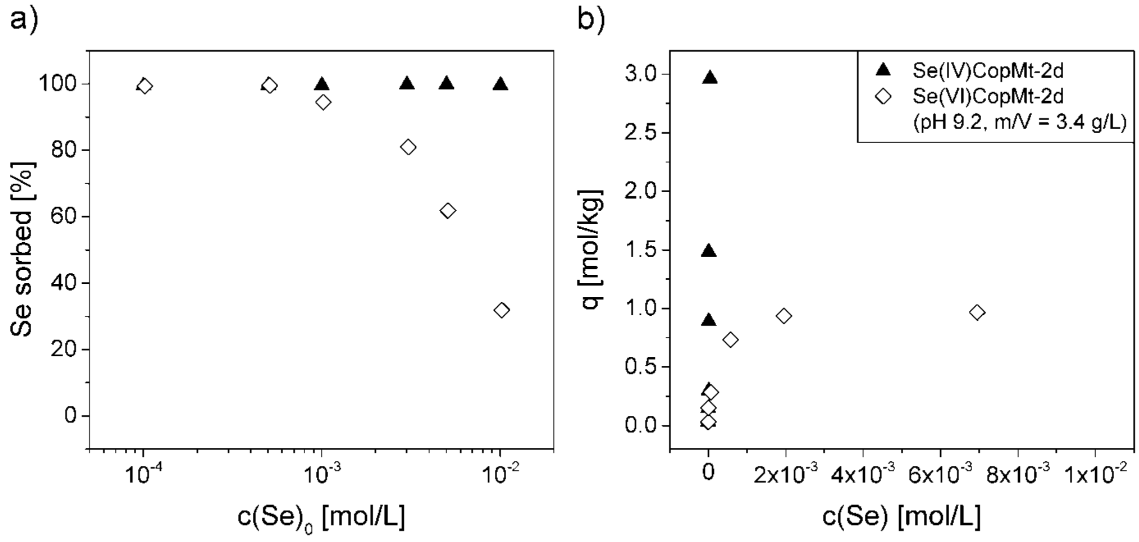

Fig. 1. Retention of Se(IV) and Se(VI) during the coprecipitation (Cop) with magnetite (Mt). (a) Se sorption as a function of the initial Se concentration, (b) Se uptake as a function of the Se equilibrium concentration.

3.3 Development of the coprecipitation products within the Fe-Se-H_2O system

Table 1 compiles the main properties of samples from coprecipitation experiments, which were conducted at different initial Se concentrations. Besides detailed hydrochemical data and the calculated Se uptake represented as both the sorbed Se percentage and the distribution coefficient (log K_d), the table contains a summarized overview of solids analysis. Regarding EDXRF results, one can observe a correlation between the total Se content of the solid phases and the initial Se concentration respectively the sorbed Se percentage. Increasing concentrations of dissolved Se(IV) or Se(VI) increase also the Se contents of the coprecipitation products, with Se(IV) causing a stronger effect than Se(VI).

Table 1. Equilibrium concentrations of Fe and Se, Se removal (in % and log K_d) and the mineral composition (Mt: magnetite, Gt: goethite, Se(0): elemental Se) of selected samples of coprecipitation experiments with different initial amounts of Se; $^{\text{“X”}}$ $c(Se)_0$ = "X" · 10^{-3} mol/L.

#	Se species	Sample	Mineral(s) [a]	Se [b] [ppm]	pH [c]	c(Fe) [mol/L]	$c(Se)_0$ [mol/L]	c(Se) [mol/L]	Se sorbed [%]	log K_d [L/kg]
1	---	Mt (pure)	Mt	bdl	8.9	7.96E-07	0.00E+00	bdl	-	-
2	Se(VI)	Se(VI)CopMt$^{0.1}$	Mt	1700	9.2	6.45E-08	1.02E-04	5.71E-07	99.4	4.72
3	"	Se(VI)CopMt$^{0.5}$	Mt + Se(0)	9900	9.1	4.16E-07	5.11E-04	2.73E-06	99.5	4.74
4	"	Se(VI)CopMt^{1}	Mt + Se(0)	16000	9.2	4.51E-07	1.02E-03	5.66E-05	94.5	3.70
5	"	Se(VI)CopMt^{3}	Mt + Se(0)	40000	9.0	1.69E-06	3.07E-03	5.84E-04	81.0	3.10
6	"	Se(VI)CopMt^{5}	Mt + Se(0)	58000	9.3	3.47E-07	5.11E-03	1.95E-03	61.9	2.68
7	"	Se(VI)CopMt^{10}	Mt + Gt + Se(0)	120000	9.1	3.28E-06	1.02E-02	6.95E-03	32.0	2.14
8	Se(IV)	Se(IV)CopMt$^{0.1}$	Mt	1700	9.2	5.23E-08	1.00E-04	5.84E-07	99.4	4.70
9	"	Se(IV)CopMt$^{0.5}$	Mt + Se(0)	8600	9.2	6.41E-08	5.02E-04	2.25E-06	99.6	4.82
10	"	Se(IV)CopMt^{1}	Mt + Se(0)	17000	9.1	2.53E-07	1.00E-03	5.10E-06	99.5	4.76
11	"	Se(IV)CopMt^{3}	Mt + Se(0)	48000	9.0	2.80E-07	3.01E-03	8.61E-06	99.7	5.01
12	"	Se(IV)CopMt^{5}	Mt + Se(0)	74000	9.3	6.56E-06	5.02E-03	1.02E-05	99.8	5.16
13	"	Se(IV)CopMt^{10}	Mt + Gt + Se(0)	140000	9.5	1.04E-06	1.00E-02	4.30E-05	99.6	4.84

[a] Mineral composition (XRD analysis). [b] Se content of the solid phase (EDXRF analysis). [c] pH after synthesis/coprecipitation

Furthermore, the analysis of the mineral composition demonstrated that, following the coprecipitation process, almost all samples contained crystalline elemental Se [Se(0)]. Se(0) could be identified by means of its characteristic peaks, which occurred in the XRD plots of all samples with higher Se contents beside the peaks of magnetite (SI Fig. A.3). Only the samples, whose total Se concentrations were too low to successfully detect the presence of Se(0) by XRD showed no signs for mineral phases other than magnetite. This indicates that the share of Se in the precipitation products is due to the presence of crystalline elemental Se. The coprecipitation of Se oxyanions and magnetite thus leads to the reduction of Se(IV) or Se(VI), resulting in the precipitation of sparingly soluble Se(0). This reductive precipitation of Se(0) does, however, not have much influence on the iron oxide formation process as neither the final pH nor the residual Fe concentration or the nature of the formed iron oxide are affected by high Se concentrations (Table 1). Solely the formation of pure magnetite is no longer possible in the case of extremely high initial Se concentrations, which instead cause the formation of magnetite-goethite mixed phases. Furthermore, samples of unsuccessful Se-magnetite coprecipitation experiments showed that the precipitation of elemental Se is not affected by the nature of the final iron oxide product. Regardless of whether the coprecipitation process leads to the formation of pure magnetite or iron(III) oxyhydroxides like goethite and lepidocrocite, formation of elemental Se can be observed (Fig. A.4).

Evaluation of the $Fe(II)/Fe_{total}$ ratio of the final coprecipitation products yielded similar results ($x_{Fe(II)}$ = 0.09 - 0.13) as those obtained for Se-free magnetite (SI Table A.1). Although the coprecipitated magnetite is affected by a partial oxidation in maghemite (cf. chapter 3.1), the oxidation process is not enhanced by the presence of dissolved Se oxyanions. Just like the Se-free magnetite, the near-surface region of the unwashed final coprecipitation products contain, besides Fe and O, certain variable amounts of C, Cl, K and Na, which indicate adsorption of dissolved ionic species or precipitation of salt phases. In addition, the final precipitates also consist of small shares of Se (~0.7 at%) resulting from the presence of elemental Se.

In order to investigate the temporal development of the coprecipitation processes within the Fe-Se-H_2O system, we analyzed samples representing different stages of the coprecipitation process. This examination included a detailed characterization of the precipitation products by XRD (Fig. 2). The results show that, at the end of the progressive oxidation (reaction time 48 hour), the coprecipitation products of both Se systems contain magnetite and elemental Se only (cf. Table 1 & SI Fig. A.3). In contrast, and as already been shown in 3.1, the precipitates that represent the early anoxic or suboxic stage of the magnetite formation process (reaction time 30 min or 3 h) consist of a number of different crystalline mineral phases. This includes iron oxides such as magnetite and green rust, (hydrogen)carbonate salts (precipitated background electrolyte) as well as elemental Se. Since the hydrochemical system contains mainly the anions chloride and (hydrogen)carbonate, it can be assumed that the green rust phase [GR] is primarily chloride green rust [GR(Cl^-)] or carbonate green rust [GR(CO_3^{2-})] (Drissi et al., 1994; Refait et al., 1998). Formation of selenite or selenate green rust (Refait et al., 2000), however, can be excluded (cf. 3.4.2).

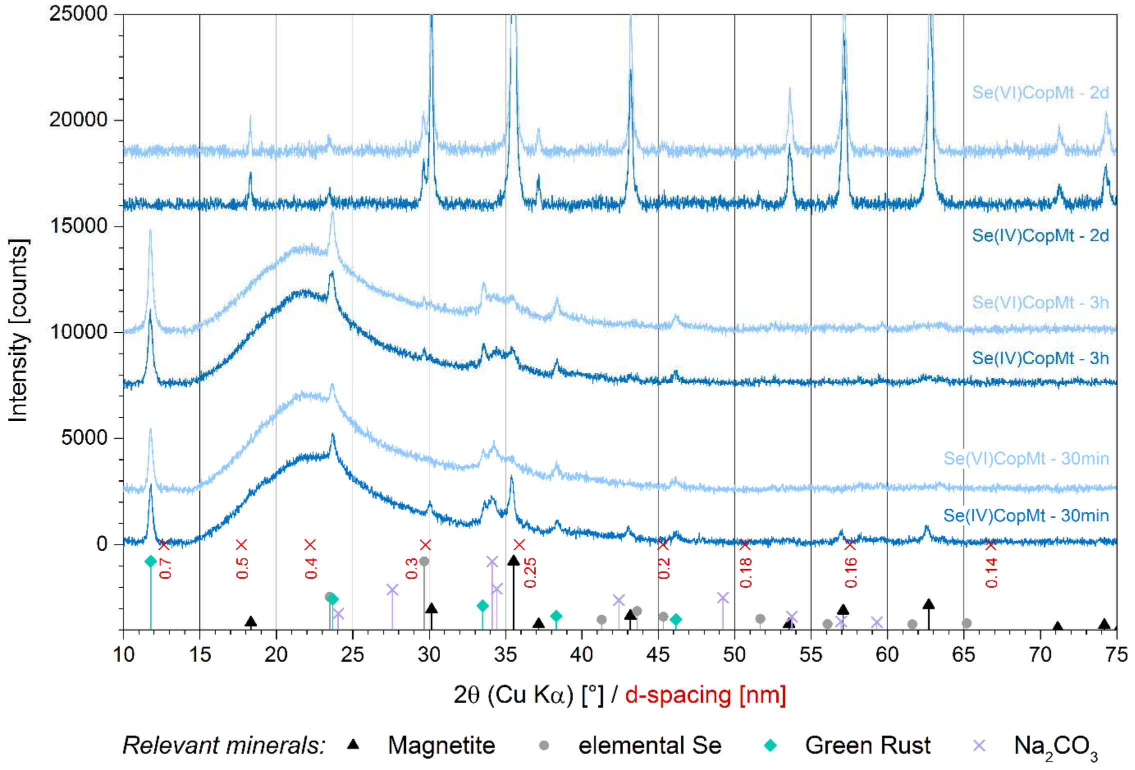

Fig. 2. Time-resolved XRD analysis of the magnetite formation pathway: At an early stage unstable green rust (GR) is present beside Mt. During the progressive oxidation, GR is completely transformed into Mt and elemental Se occurs as a separate mineral phase.

The short-term samples presumably also contain amorphous or poorly crystalline iron(II) hydroxide, which might be responsible for the broad peak in the XRD plot. That the short-term coprecipitation samples mainly consist of iron hydroxides rather than iron oxides could be confirmed by the analysis of the O 1s spectra. Based on the comparison of the measured O 1s binding energies with references, the dominance of hydroxide (OH^-) over oxide (O^{2-}) compounds could be illustrated (SI Fig. A.5). Due to this dominance of iron hydroxides, it was, however, not possible to apply the previous described evaluation procedure for the determination of $x_{Fe(II)}$ (cf. chapter 3.1). In order to estimate the Fe(II)/Fe$_{total}$ ratio, the Fe 2p spectra of the analyzed coprecipitation samples were therefore directly compared with the published Fe 2p spectra of stoichiometric GR(CO_3^{2-}) [$Fe^{II}_4Fe^{III}_2(OH)_{12}CO_3 \cdot 3\ H_2O$; $x_{Fe(II)} = 0.67$] (Mullet et al., 2008). Since the Fe 2p spectra are almost identical (SI Fig. A.5), one can assume that the proportion of Fe(II) lies also in the range of $x_{Fe(II)} = \sim 0.67$ (SI Table A.1).

Regarding the mineral composition as well as the relative proportions of the minerals (estimated from peak intensities), there is hardly any difference between reaction times of 30 min or 3 h. The only exceptions are elemental Se, which can only be identified in the samples with a reaction time of 3 hours, and the GR phase, whose fraction seems to increase (Fig. 2). The relatively large proportion of green rust in the short-term coprecipitation samples (30 min and 3 h) is particularly noticeable in comparison to the equivalent samples of the Se-free system, which show scarcely any evidence of GR (cf. SI Fig. A.1). Precipitation of GR therefore appears to be associated with the presence of dissolved Se oxyanions.

Furthermore, since the proportion of magnetite does not increase within the first 3 hours, one can conclude that the magnetite formation requires a certain period of time. This is also confirmed by the macroscopic observation that the color change of the precipitate from bluish green to black lasts several hours. Formation of magnetite is thus the result of the progressive oxidation of the system, which causes the complete transformation of the primarily formed Fe(II)-rich iron oxide phases into magnetite. It is known that both iron(II) hydroxide and GR are only stable under anoxic conditions and are oxidized to magnetite or iron(III) oxyhydroxides like goethite or lepidocrocite in contact with air or dissolved oxygen, respectively (Drissi et al., 1994; Schwertmann and Fechter, 1994). The nature of the oxidation product thereby depends on the general hydrochemical conditions, whereby low oxidation rates as well as an alkaline pH favor the formation of magnetite (Drissi et al., 1994; Perez et al., 1998; Refait et al., 1998; Perez and Umetsu, 2000; Sumoondur et al., 2008).

3.4 Reductive precipitation of Se oxyanions

Precipitation of elemental Se could also be verified by SEM/EDX and XPS results. SEM images of two analyzed samples from each Se system – Se(IV) or Se(VI) – are shown in Figure 3 and SI Figure A.6 & A.7, respectively. These samples were selected because of their high Se content (6 - 7 wt%), arising from initial Se(IV) or Se(VI) concentrations of $5 \cdot 10^{-3}$ mol/L. The images of both samples indicate the formation of elongated (1 - 2 µm) euhedral Se(0) crystals (identified via EDX; SI Fig. A.6 or A.7) that are embedded in the magnetite matrix. Although the Se(0) crystals vary in size, they are all significantly larger than the magnetite particles with average sizes of 25 - 50 nm. Moreover, the XPS analysis prove that, at the end of the 48-hour reaction time [SeCopMt], Se is present in the oxidation state Se(0) (SI Table A.1). This confirms the previous findings, according to which the coprecipitation of Se(IV) or Se(VI) with magnetite ends in the formation of elemental Se.

That interaction between reduced Fe minerals and Se oxyanions can cause a reductive Se precipitation and hence a Se immobilization was also observed in previous publications. Formation of Se(0) was demonstrated by studies regarding Se(IV) or Se(VI) reduction by ZVI (Liang et al., 2013; Tang et al., 2014) or Fe(II)-bearing mineral phases like iron(II) hydroxide

(Murphy, 1988; Zingaro et al., 1997; Chen et al., 2009) and green rust (Myneni et al., 1997; Johnson and Bullen, 2003; Scheidegger et al., 2003). By contrast, sorption studies on magnetite (Scheinost et al., 2008; Scheinost and Charlet, 2008) showed that reduction processes can also lead to the formation of various iron selenide compounds. This also applies to an interaction of Se(VI) with nanoparticulate ZVI (Olegario et al., 2010). However, even under consistently anoxic conditions, interaction of Se oxyanions with reduced Fe phases does not always cause a reductive Se precipitation, which was confirmed in several sorption studies (Loyo et al., 2008; Jordan et al., 2009; Missana et al., 2009). Concerning the Se reduction process, this suggests that the formation pathway of magnetite and the other involved iron oxide phases plays a crucial role.

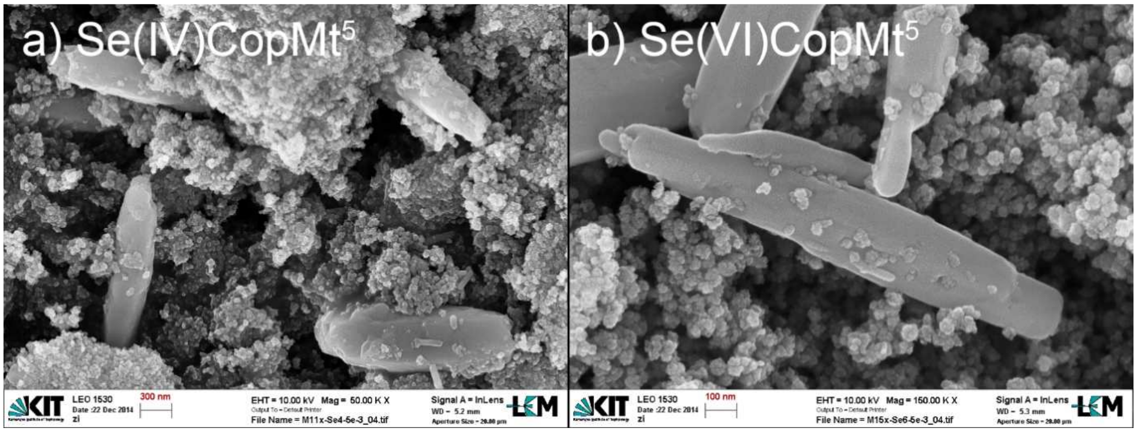

Fig. 3. SEM images of coprecipitation products consisting of large, lath-shaped elemental Se crystals in the matrix of magnetite aggregates. (a) Se(IV)-magnetite coprecipitation; (b) Se(VI)-magnetite coprecipitation. $c(Se)_0 = 5 \cdot 10^{-3}$ mol/L.

In addition, the time-resolved analysis of the coprecipitation process shows that elemental Se occurs for the first time after 3 hours and that the intensity of the Se(0) peaks and hence the relative Se(0) content increases in the subsequent period (Fig. 3). The formation of Se(0), therefore, does not take place in the very beginning of the coprecipitation process, but only at a later stage. Indications for the presence of crystalline Se-bearing minerals other than Se(0) are not visible.

The results of the development of the residual Se concentrations, however, clearly demonstrate that most of the initial Se(IV) or Se(VI) content is already removed from solution after reaction times of 30 min (Fig. 4). This is confirmed by the XPS results of the respective solid samples [SeCopMt-30min], whose chemical composition show significant shares of Se. The analysis of the dissolved Se concentration also illustrates that no Se is released during the Se(0) formation, or during the transformation of the iron hydroxides into magnetite.

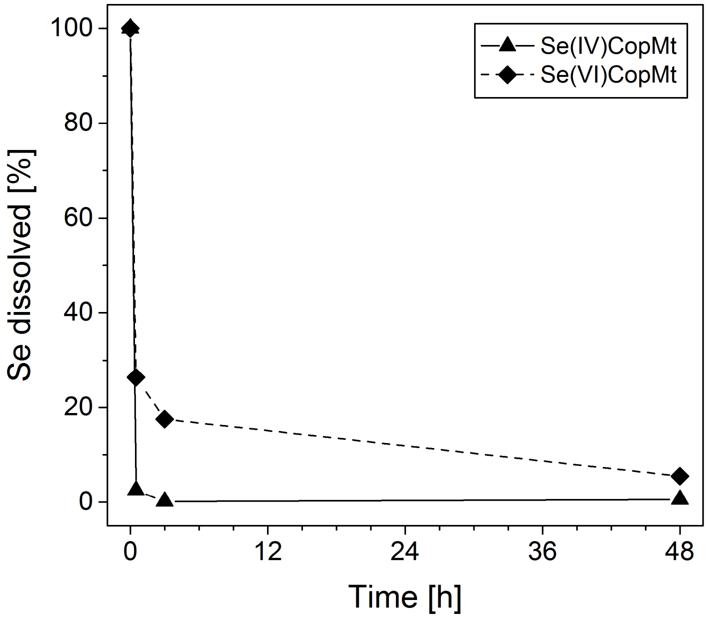

Fig. 4. Evolution of the Se(IV) or Se(VI) concentration during the coprecipitation process.

In order to find out what retention mechanism causes the immobilization of Se(IV) or Se(VI) in the early stage of the coprecipitation process, the fate of Se after reaction times of 30 min was characterized in detail. This included, among other things, an analysis of the Se oxidation state by the determination of the Se binding energies via XPS (SI Table A.1). The results prove that the precipitates representing the early coprecipitation stage [SeCopMt-30min] contain Se in the oxidation stage Se(-II). Reduction of Se(IV) and Se(VI) thus takes place within the first minutes of the coprecipitation, in a period in which the dissolved Se oxyanions are in contact with the Fe(II)-rich precursor phases of magnetite under anoxic conditions.

In addition, the absence of Se(IV) or Se(VI) demonstrates that the retention is not due to adsorption processes, which means, that the fast removal of Se oxyanions is not associated with the rapid adsorption kinetic of Se oxyanions on iron oxide minerals (Rovira et al., 2008; Loyo et al., 2008; Missana et al., 2009; Mitchell et al., 2013). The same also applies to Se immobilization due to the formation of selenite or selenate GR or the incorporation of Se oxyanions in magnetite or its precursor phases. That the coprecipitation between magnetite and dissolved oxyanions can generally lead to an incorporation was demonstrated by Wang et al. (2011) for the oxyanion As(V). Up to now, however, there is no evidence that comparable processes could also be relevant for the Se(IV)-magnetite or Se(VI)-magnetite system.

S/TEM in combination with EDX analyses enabled a spatially resolved optical and chemical characterization of a Se(-II)-bearing coprecipitation sample [Se(IV)CopMt-30min]. Figure 5 shows a HAADF image together with relevant elemental mappings.

Regarding the mineral composition, the TEM/EDX analysis confirms the previous results, according to which the primary precipitation products consist of different mineral phases. These are primarily iron minerals and, in particular, iron oxides. The analyzed sample contains crystalline as well as amorphous or poorly crystalline phases, whereby the relatively large GR particles are particularly striking. GR crystals can be identified by their distinctive hexagonal crystal shape (Legrand et al., 2004; Génin et al., 2006). Since they are characterized by higher levels of chloride, it is also possible to identify GR particles that are positioned vertically. The higher chloride contents suggest that the GR phase is primarily GR(Cl^-). In this context, one has however to consider that the analysis of carbon and therefore the detection of GR(CO_3^{2-}) was not possible via EDX due to the C-containing TEM grid. Elements such as Na and K show a homogeneous distribution and their occurrence is not connected with particular mineral phases. This indicates that the major part of Na and K is adsorbed on the surface of iron oxide minerals.

Unlike Na und K, the distribution of Se is extremely heterogeneous. There are no signs that spots with high Se concentrations are associated with certain iron oxide minerals. EDX spectra of Se-rich spots are characterized by high Se and Fe contents, while their proportion of O tends to be lower than for Se-free spots. The latter can be seen in SI Fig. A.8, which includes a comparison between the EDX spectrum of an isolated Se-rich spot and the spectrum of the center of a GR particle, containing mainly Fe, O, and small amounts of Cl. Therefore, higher Se concentrations are likely associated with the occurrence of iron selenide compounds. These compounds are present in the iron oxide matrix in the form of heterogeneously distributed independent mineral phases. Moreover, with sizes below 100 nm, these iron selenide particles are also rather small.

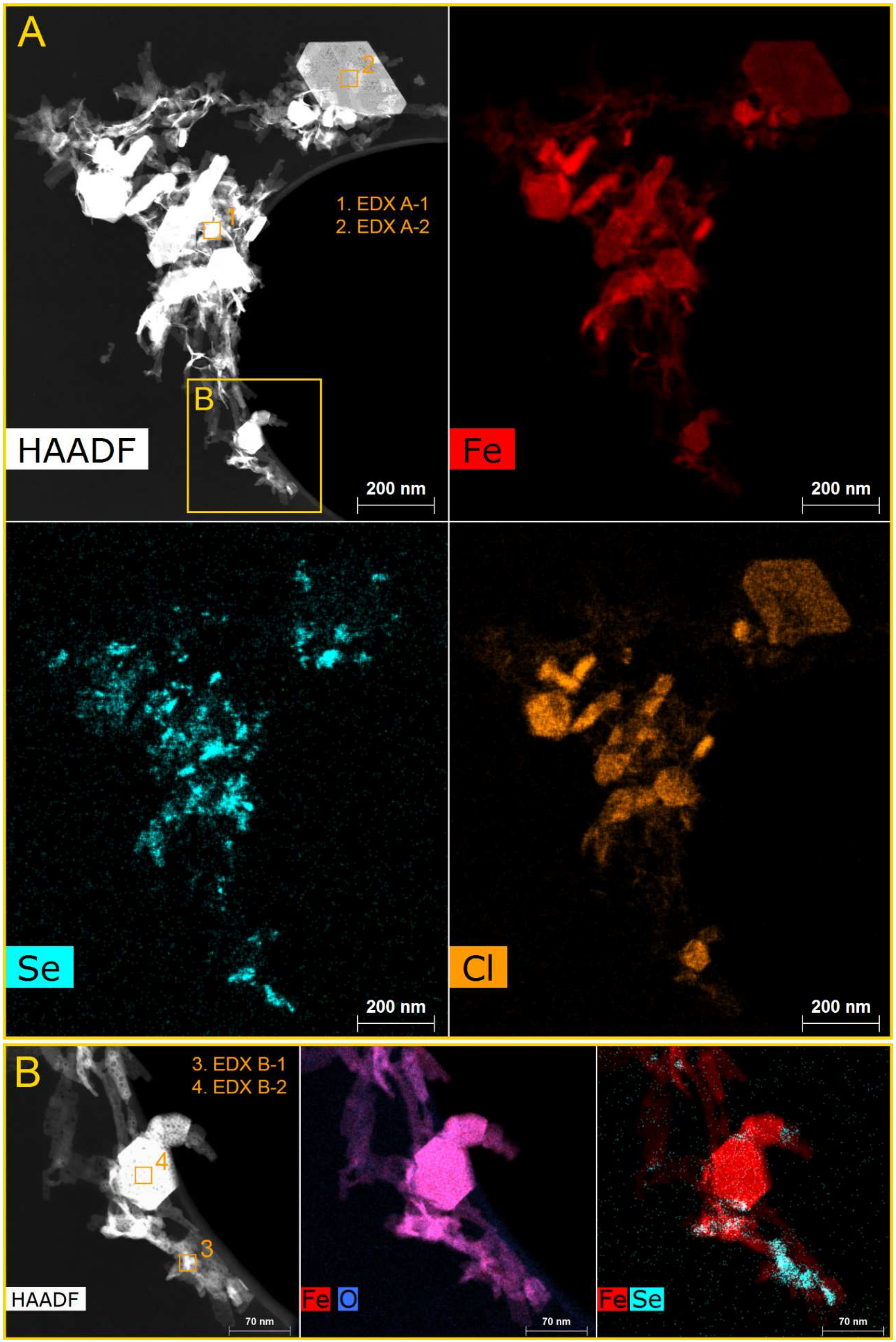

Fig. 5. **HAADF images and elemental mappings of a Se(IV)-magnetite coprecipitation product after a reaction time of 30 min. EDX spectra of the marked spots are shown in Fig. A.8.**

3.5 Temporal evolution of the Se speciation

Results of Se K-edge XAS analyses were used to characterize the Se oxidation state (XANES) as well as the nature of the local Se structure (EXAFS) during the coprecipitation process. For this purpose, coprecipitation products of both Se systems were analyzed after reaction times of 30 min, 3 h and 48 h (cf. samples Fig 2).

Figure 6 shows the Se K-edge XANES spectra of the analyzed samples together with reference spectra of the minerals ferroselite [$FeSe_2$], achavalite [FeSe], and, gray elemental Se [Se(0)]. A comparison of the reference spectra illustrates that the oxidation states Se(0), Se(-I), and Se(-II) are difficult to differentiate based on the very similar position of their absorption edge (12.6553 - 12.6560 keV). However, they can be easily distinguished based on the characteristic shape of the white line. While the white line of gray Se(0) is dominated by one significant peak, the white line of ferroselite and achavalite is of lower intensity and, in case of achavalite, also characterized by two maxima. Just like achavalite, the samples with reaction times of 30 min [SeCopMt-30min] show white lines of relatively low intensities and two maxima, confirming that Se is indeed present in the form of Se(-II). These XANES data are thus in line with the previous findings of the XPS analysis after which dissolved Se(IV) and Se(VI) oxyanions are reduced to Se(-II) in the early stage of the coprecipitation process.

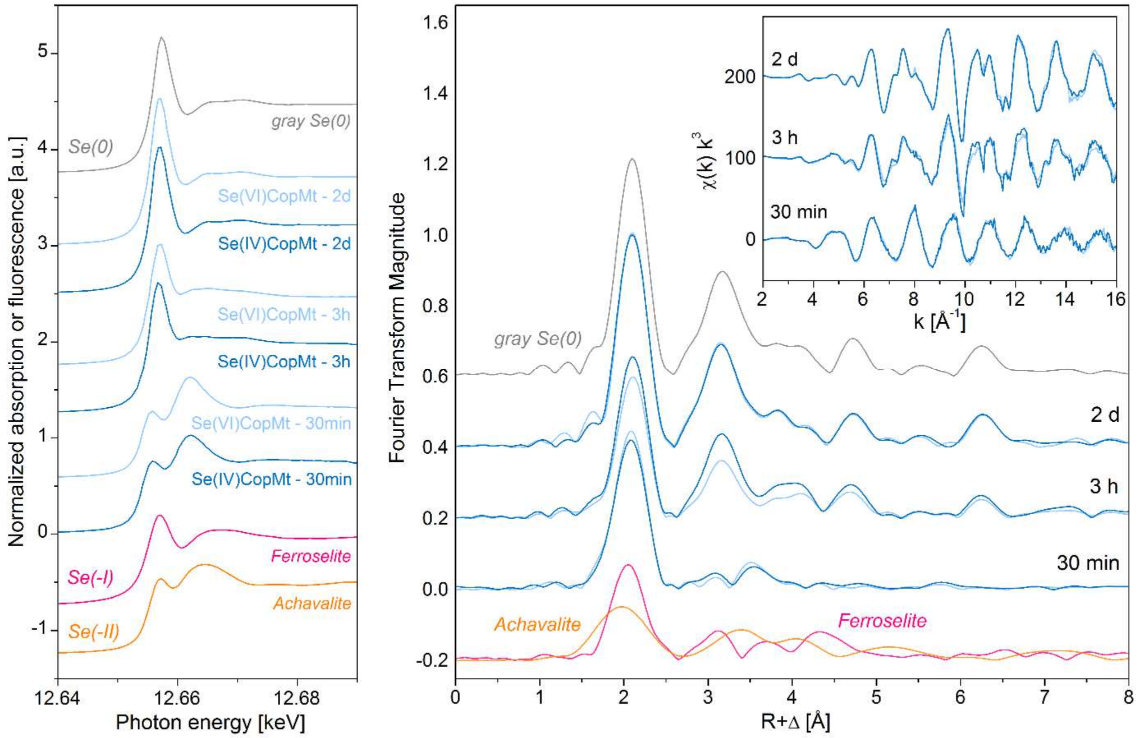

Fig. 6. Se K-edge XANES and EXAFS spectra of Se-magnetite coprecipitation products of different reaction times and various Se references.

However, during the oxidation of the system, these Se(-II) species are afterwards transformed to elemental Se, as can be seen from the high similarity between the white lines of gray Se and the coprecipitation samples with reaction times of 3 hours [SeCopMt-3h] and 2 days [SeCopMt-2d]. In this form, the Se stays stable, although Se(0) does not represent the thermodynamically most stable oxidation state under oxic conditions. Furthermore, there is no difference between samples of the Se(IV) and Se(VI) system, indicating that at no time of the oxidation process the Se solid state speciation is influenced by the initial aqueous speciation.

Regarding the Se binding structure, a comparison of the EXAFS Fourier transforms (FT) illustrates that spectra of the Se(0)-bearing samples are identical to the gray Se reference, whereas the EXAFS FT magnitude of the Se(-II) species is clearly different from reference spectra of achavalite or ferroselite (Fig 6). In order to check whether the samples with reaction times of 3 hours represent a spectral mixture of Se(-II) and Se(0) species, a statistical analysis was performed using Iterative Transformation Factor Analysis (ITFA) (Rossberg et al., 2003; Scheinost and Charlet, 2008). This ITFA included the EXAFS spectra of all coprecipitation samples as well as the spectrum of gray Se, since the previous results showed that the immobilized Se should be present as gray Se at the end of the coprecipitation process. Fig. 7a shows the excellent match between the experimental spectra (black lines) and their reconstructions (red or blue lines) by two principal components (PC). The Varimax factor loadings (Fig 7b) demonstrate that the gray Se reference as well as the final coprecipitation products [SeCopMt-2d] are solely dominated by PC 1, without any influence of PC 2. PC 1 therefore represents the occurrence of elemental gray Se. By contrast, samples of the early stage [SeCopMt-30min] are characterized only by PC 2, epitomizing the the Se(-II) phase. In addition, as the samples of the intermediate stage [SeCopMt-3h] are described by both principal components, one can conclude that these samples contain indeed both different types of Se species. Due to the limited radial resolution of EXAFS, only the samples representing the Se(0) and Se(-II) endmembers were fitted (Table 2).

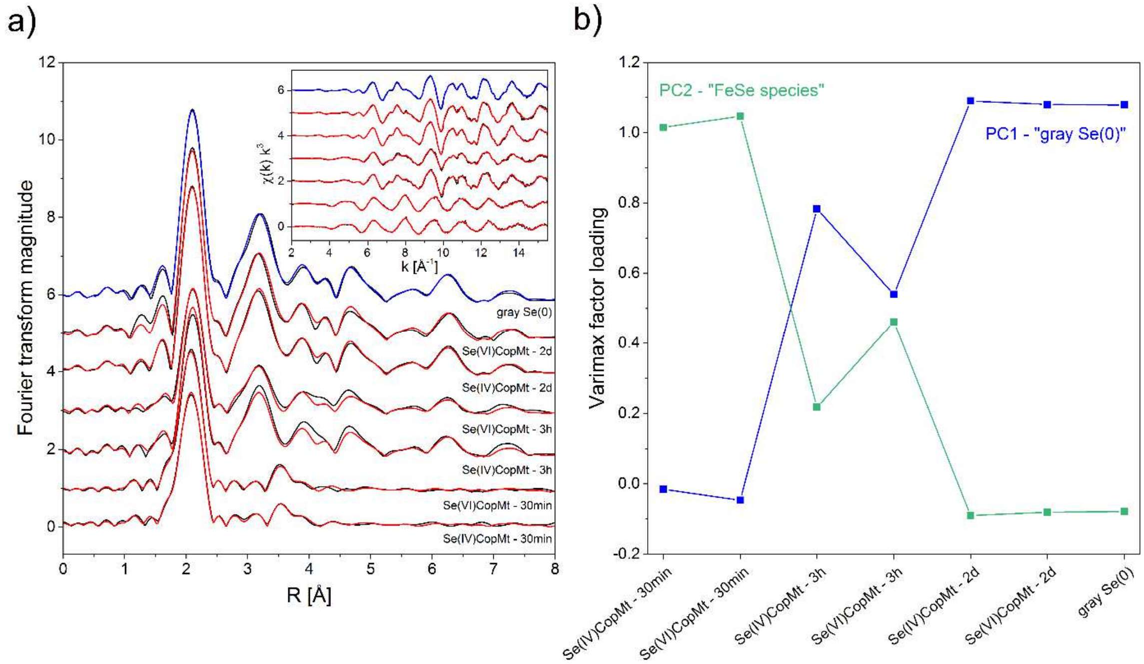

Fig. 7. (a) Se K-edge EXAFS spectra of Se-magnetite coprecipitation products of different reaction times and of a gray Se(0) reference. Experimental spectra are shown as black lines, their reconstruction by two factors as red or blue lines. (b) Varimax loadings of the two factors.

For the Se(-II)-bearing samples, the k^3-weighted χ spectra were fit with a FEFF 8.2 file generated with the crystallographic structure of tetragonal iron(II) selenide (FeSe, CIF 26889). The EXAFS FT magnitude of these samples is dominated by a strong peak at 2.1 Å (uncorrected for phase shift). This peak could be well fitted with a single scattering Se-Fe path, resulting in iron coordination numbers (CN) of 2.7 - 2.8 and atomic distances of 2.40 Å. The use of a Se-Se path, in contrast, led to poor fit results, hence can be excluded. In case of the structural features in the EXAFS FT range between 3.1 - 3.5 Å (uncorrected for phase shift), three individual single scattering Se-Fe and Se-Se paths had to be used to achieve a good fitting. This resulted in further shells of approximately 1 Se atom at 3.39 Å, 5 - 6 Se atoms at 3.90 Å and 2 - 3 Fe atoms at 4.12 Å (Table 2). A comparison with the known crystal structures of the iron selenides dzharkenite, ferroselite, achavalite, tetragonal FeSe, Fe_3Se_4 or Fe_7Se_8 (Scheinost et al., 2008) demonstrates that none of these minerals match the observed atomic distances of the Se(-II) species within the reduced samples. The highest similarity shows tetragonal FeSe, which is characterized by a Fe coordination shell at 2.37 Å and neighboring Se atoms in a distance of 3.91 Å. However, while unlike tetragonal FeSe, the reduced samples show no Se shell at approximately 3.77 Å, the documented Se and Fe shells at 3.38 Å and 4.12 Å, respectively, are missing in case of tetragonal FeSe (Scheinost and Charlet, 2008).

The general observation that the structure of a Se reduction product, resulting from an interaction with reduced iron, shows similarities with tetragonal FeSe was also observed in EXAFS studies by other authors (Scheinost et al., 2008; Scheinost and Charlet, 2008; Loyo et al., 2008; Olegario et al., 2010). Like in our study, the fit results of reduction products showed a Fe coordination shell in a distance of 2.34 - 2.42 Å and Se neighbors at 3.87 - 4.02 Å (Scheinost et al., 2008; Loyo et al., 2008; Olegario et al., 2010). Moreover, some of these authors also found additional Se and Fe shells similar to the observed Se shell at 3.38 Å (Scheinost and Charlet, 2008; Loyo et al., 2008) or Fe shell at 4.12 Å (Scheinost et al., 2008), which are missing in the case of tetragonal FeSe. In addition, all EXAFS results have in common that the coordination numbers of the Fe and Se shells are much smaller than the ones of crystalline iron selenide minerals. This suggests that the reductive precipitation of Se oxyanions leads to the formation of an iron selenide phase [FeSe] with particle sizes in the nanometer range (Scheinost et al., 2008; Scheinost and Charlet, 2008; Loyo et al., 2008; Olegario et al., 2010). Even though these FeSe nanoparticles are characterized by a short-range structure, their binding structure is different from that of macrocrystalline FeSe minerals like achavalite or tetragonal FeSe. The theory of the formation of nanoparticulate FeSe is also strongly supported by the TEM results, providing the first direct evidence that the FeSe particles are smaller than 100 nm. Furthermore, the presence of poorly crystalline FeSe nanoparticles would explain why the FeSe phase could not be detected by XRD.

Table. 2 Se-K XANES edge energies and EXAFS fit results of Se-magnetite coprecipitation products of different reaction times (S_0^2 = 0.9).

		Coordination shell				Further shells					
Sample	E_0 [keV]	CN[a]		R [Å][b]	σ^2 [Å^2][c]	CN		R [Å]	σ^2 [Å^2]	ΔE_0 [eV]	χ^2_{res} [%]
Se(IV)CopMt[1]-30min	12.6541	2.7	Fe	2.40	0.0037	1.0	Se	3.39	0.0066	12.7	4.3
						5.3	Se	3.89	0.0100 [§]		
						2.4	Fe	4.11	0.0074		
Se(VI)CopMt[1]-30min	12.6540	2.8	Fe	2.40	0.0036	0.5	Se	3.38	0.0052	12.9	3.6
						6.1	Se	3.90	0.0100 [§]		
						2.6	Fe	4.13	0.0070		
Se(IV)CopMt[1]-2d	12.6556	2 [f]	Se	2.38	0.0015	4 [f]	Se	3.38	0.0047	10.6	3.8
						2 [f]	Se	3.74	0.0034		
						6 [f]	Se	4.32	0.0058		
						4 [f]	Se	4.46	0.0046		
						4 [f]	Se	4.94	0.0048		
Se(VI)CopMt[1]-2d	12.6556	2 [f]	Se	2.38	0.0015	4 [f]	Se	3.38	0.0046	10.9	4.2
						2 [f]	Se	3.74	0.0036		
						6 [f]	Se	4.31	0.0061		
						4 [f]	Se	4.45	0.0049		
						4 [f]	Se	4.94	0.0050		

[a] CN: coordination number, error ± 25%. [b] R: Radial distance, error ± 0.01 Å. [c] σ^2: Debye-Waller factor, error ± 0.0005 Å^2.
[f] fixed coordination numbers. [§] Upper σ^2 limit reached. ["X"] $c(Se)_0$ = "X" · 10^{-3} mol/L.

The fit of χ spectra of the Se(0)-bearing samples was performed with a FEFF 8.2 file generated with the crystallographic structure of gray Se (Se trigonal, CIF 22251). As the previous results have already shown that Se is most likely present as gray Se in these samples, we used the first 6 single scattering Se-Se paths of this Se reference with fixed coordination numbers for the fitting (Table 2). The perfect fit and the corresponding interatomic Se distances clearly show that the Se species in these samples is indeed crystalline gray Se.

That reduction of Se oxyanions by reduced iron can result in the formation of trigonal, gray Se was also demonstrated in studies with iron(II) hydroxide (Zingaro et al., 1997), siderite (Scheinost et al., 2008), or ferrous iron sorbed on clay minerals (Charlet et al., 2007). Other publications, however, reported the formation of amorphous elemental Se. This includes studies about the reduction potential of green rust minerals (Myneni et al., 1997; Scheidegger et al., 2003). In addition, Scheinost and Charlet (2008) showed that reduction of Se(IV) by mackinawite caused the formation of nanoparticulate red Se.

3.6 Conceptual model of the Se retention during the magnetite formation

The results of this study prove that the immobilization of Se oxyanions during the aerial oxidation of an anoxic Fe-Se-H_2O system, which results in the formation of magnetite, is due to two redox processes.

The first redox process takes place under reducing conditions in the early stage of the magnetite formation, where dissolved Se oxyanions interact with primarily Fe(II)-rich precipitation products of the aquatic Fe^{2+} system. These products are mainly iron(II) hydroxide and green rust, which represent the unstable precursor phases of the later formed magnetite. This interaction leads to a reduction of Se(IV) or Se(VI) to Se(-II) and causes the formation of nanoparticulate iron selenide (FeSe) phase. At the same time, the involved iron(II) hydroxide phases are transformed to Fe(III)-rich minerals, due to the corresponding oxidation of Fe(II) to Fe(III) during this reductive Se precipitation (Fig. 8).

It is known that the reduction of dissolved Se oxyanions by Fe(II) requires the presence of Fe(II) mineral phases and the reaction with their active mineral surfaces (Chen et al., 2009). Although the presence of dissolved Fe^{2+} generally favors the Se reduction process (Tang et al., 2014), a reduction only by dissolved Fe^{2+} is not possible due to the difference in reduction potentials of the redox couples (Chakraborty et al., 2010), Responsible for the Se reduction is most likely the interaction with iron(II) hydroxide and its subsequent oxidation to green rust, since the occurrence of larger amounts of green rust is directly related to the presence of dissolved Se oxyanions. Thus, only the reductive Se precipitation by iron(II) hydroxide and the associated production of Fe(III) makes the formation of an iron(II,III) mineral like green rust possible under the prevailing anoxic condition. Regarding the formation of GR(Cl^-), the corresponding redox reaction would be:

$$28\,Fe^{II}(OH)_2 + SeO_4^{2-} + 8\,Cl^- + 5\,Fe^{2+} + 4\,H_2O \rightarrow 8\,Fe_3^{II}Fe^{III}(OH)_8Cl + FeSe$$

$$21\,Fe^{II}(OH)_2 + SeO_3^{2-} + 6\,Cl^- + 4\,Fe^{2+} + 3\,H_2O \rightarrow 6\,Fe_3^{II}Fe^{III}(OH)_8Cl + FeSe$$

As can be seen from these equations, the quantity of available iron(II) hydroxide determines the total amount of immobilized Se(IV) or Se(VI). Since the reduction of Se(VI) to FeSe requires more iron(II) hydroxide than the reduction of Se(IV), the amount of reduced Se(IV) is always higher at a specific Se/Fe^{2+} ratio. However, the amount of immobilized Se also depends on the reduction kinetics, whereby particularly the reduction step of Se(VI) to Se(VI) is kinetically hindered (Séby et al., 1998; De Cannière et al., 2010).

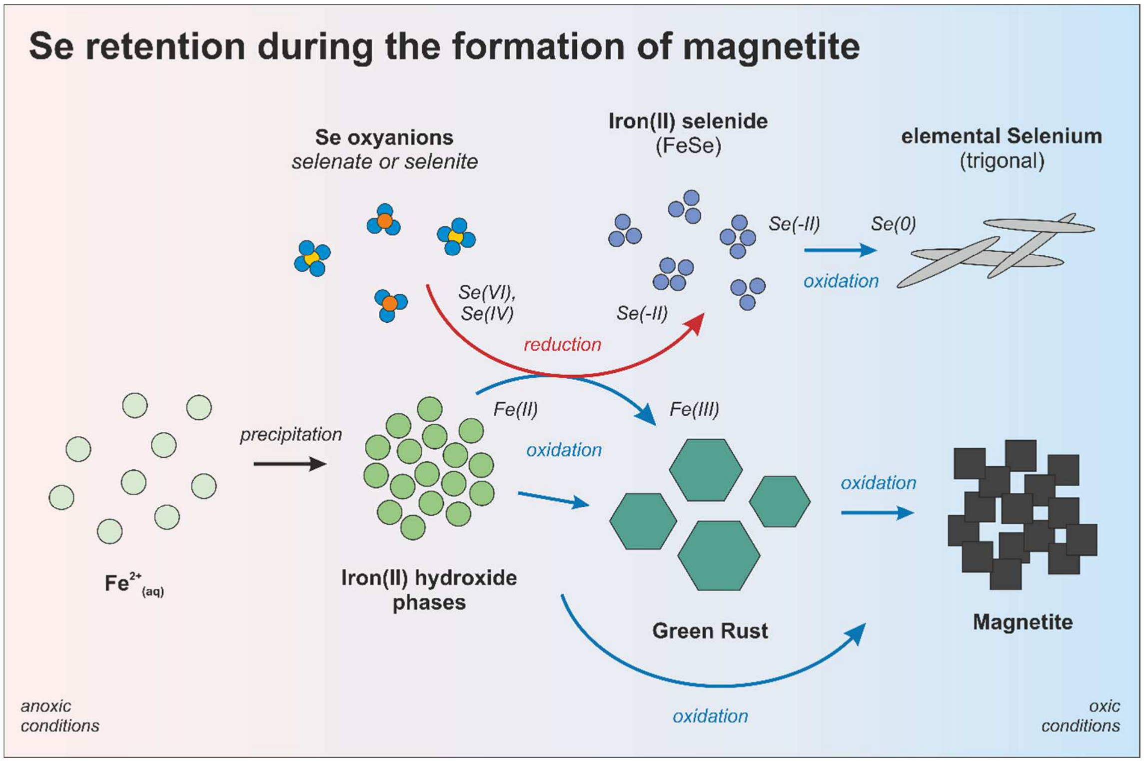

Fig. 8. Schematic representation of the retention of Se oxyanions during the formation of magnetite.

Concerning the question why the reduction of Se oxyanions sometimes causes the formation of FeSe and sometimes of elemental Se, Scheinost et al. (2008) postulated a theory according to which the type of precipitation product is linked to the reduction kinetics. While formation of iron selenides is only possible in case of fast reduction kinetics, a slow Se reduction favors the precipitation of elemental Se. In general, the reduction kinetics is directly related to the particle sizes and morphology of the interacting Fe(II)-bearing mineral phases. A fast Se reduction is therefore only possible in case of relatively small particles with high specific surface areas (Scheinost et al., 2008; Scheinost and Charlet, 2008). Since the Se reduction process mainly takes place within the first 30 minutes and through the interaction with iron(II) hydroxide and green rust, which are both characterized by small particle sizes and/or high specific surface areas, the results of this study are consistent with the theory that the reduction kinetics defines the Se precipitation product.

Moreover, Kang et al. (2013) found that the total amount of Se oxyanions plays an important role in this context. This is due to the fact that shares of remaining non-reduced Se oxyanions prevent the precipitation of FeSe and support the formation of elemental Se:

$$SeO_3^{2-} + 2\,FeSe + 6\,H^+ \rightarrow 3\,Se(0) + 2\,Fe^{2+} + 3\,H_2O$$

$$SeO_4^{2-} + 3\,FeSe + 8\,H^+ \rightarrow 4\,Se(0) + 3\,Fe^{2+} + 4\,H_2O$$

However, because of the alkaline pH as well as the relatively large amount of Fe(II) mineral phases, resulting in a small amount of remaining Se oxyanions, one can assume that this reaction is prevented in our studies.

The second important Se redox reaction takes place during the progressive oxidation of the aquatic system due to the contact with atmospheric oxygen. This process leads to further oxidation of Fe(II) to Fe(III) and thereby to the complete transformation of iron(II) hydroxide and green rust into magnetite. Besides that, however, oxygen also causes the oxidation of Se(-II) to Se(0). As a consequence, the nanoparticulate FeSe oxidizes to gray elemental Se that occurs in form of euhedral crystals with sizes of 1 - 2 µm within the magnetite matrix (Fig. 8). The oxidation of FeSe in elemental Se can generally be described by the following two-part dissolution-precipitation reaction:

$$FeSe + H^+ \rightarrow Fe^{2+} + HSe^-$$

$$HSe^- + 0.5\,O_2 + H^+ \rightarrow Se(0) + H_2O$$

As can be derived from this reaction, formation of microcrystalline gray Se from nanoparticulate FeSe should only be possible when O_2 reacts primarily with the iron hydroxide phases and not with FeSe. Otherwise it is hard to explain how the HSe^- remains stable long enough to form Se(0) particles of larger sizes. However, if the entry of O_2 causes the oxidation of the iron hydroxides, this would result in a buffering of the system and in the preservation of the initial anoxic conditions. Kurokawa and Senna (1999) reported a self-stabilization effect of green rust against aerial oxidation by adsorption of dissolved Fe^{2+}. This oxidation process would then inevitably lead to a consumption of Fe^{2+}, which in turn would cause the dissolution of the most unstable Fe(II) mineral phases. In this context, dissolution of the nanoparticulate FeSe comes into question, since FeSe has a relatively high solubility compared to other iron selenides or iron(II) hydroxides (Kang et al., 2013). Furthermore, it is known that the solubility of nanoparticulate phases can be significantly higher than for crystalline particles of larger sizes (Fernández-Martínez and Charlet, 2009). Due to the still prevailing anoxic conditions, the hereby formed HSe^- species would be stable for a longer time. This would allow a more controlled and slower Se(-II) oxidation and thus the formation of elemental Se with larger particle sizes.

It must also be noted that elemental Se is still the dominant Se phase at the end of the coprecipitation process, even though Se(0) is not the thermodynamically favored oxidation state under alkaline, oxic conditions. This is probably influenced by the relatively large size of the elemental Se crystals that inhibits further oxidation of Se(0). Since the progressive oxidation is not accompanied by remobilization of Se and there is also no indication of a further Se oxidation, the stability of the Se immobilization seems to be mainly determined by the previous transformation of unstable FeSe into elemental Se. Interestingly, the Se retention mechanism is also not affected by the nature of the final iron oxide precipitation product (Fig. A.4). Dissolved Se oxyanions are initially reduced to FeSe and then oxidized to elemental gray Se, regardless of whether the oxidation of iron(II) hydroxide and green rust leads to the formation of magnetite or iron(III) oxyhydroxides like goethite and lepidocrocite.

4 Conclusion

The results of this study demonstrate that the formation pathway of magnetite is more crucial for the immobilization of dissolved Se oxyanions than the interaction processes after the completed mineral formation. Key factor is the contact and interaction of Se oxyanions with metastable Fe(II)-rich intermediates, which causes a reductive Se precipitation and defines the retention capacity. Also of great importance are the prevailing hydrochemical conditions, including pH and redox, since those parameters primarily determine the iron oxide formation and transformation pathway as well as the nature and stability of the Se precipitation products. In case of the here investigated conditions, this behavior led to the initial reduction of Se(IV) or Se(VI) to FeSe, which was afterwards oxidized to elemental gray Se during the progressive aerial oxidation process.

Regarding the behavior of Se in the geosphere, the study showed that reductive Se precipitation represents an efficient and comparatively durable mechanism to immobilize dissolved Se oxyanions. Processes like these should be considered in safety assessments of HLW disposal sites, as they may affect the migration of the radionuclide ^{79}Se (interaction of ^{79}Se with secondary iron oxides in the near-field). Moreover, one could imagine that this mechanisms are used actively to reduce the appearance of mobile Se species. An intended manipulation of the redox-dependent Se solubility due to the entry of reduced iron could, for example, be applied in the treatment of Se contaminated wastewaters.

Acknowledgements

This work is part of the *IMMORAD* project, funded by the German Federal Ministry for Education and Research (BMBF) under grant No. 02NUK019B. Additional financial support was provided by the Graduate School for Climate and Environment (GRACE) at KIT. The authors would like to thank Dr. Arne Jansen and Volker Zibat for S/TEM and SEM analysis, Dr. Peter Weidler for BET determination and Dr. Jörg-Detlef Eckhardt for assistance with XRD analysis. We also thank Dr. Utz Kramar and Claudia Mößner for their help during XRF and ICP-MS analysis. The ESRF and the team of the Rossendorf Beamline (BM 20) are gratefully acknowledged for the provision of beam time and their support during the XAS measurements.

References

Ankudinov A. L. and Rehr J. J. (1997) Relativistic calculations of spin-dependent x-ray-absorption spectra. *Phys. Rev. B* **56**, 1712–1715.

Bingham P. A., Connelly A. J., Cassingham N. J. and Hyatt N. C. (2011) Oxidation state and local environment of selenium in alkali borosilicate glasses for radioactive waste immobilisation. *J. Non. Cryst. Solids* **357**, 2726–2734.

Blume H.-P., Brümmer G. W., Fleige H., Horn R., Kandeler E., Kögel-Knabner I., Kretzschmar R., Stahr K. and Wilke B.-M. (2016) *Scheffer/Schachtschabel - Soil Science*. 16th ed., Springer, Heidelberg, Germany.

Börsig N., Scheinost A. C., Shaw S., Schild D. and Neumann T. (2017) Uptake mechanisms of selenium oxyanions during the ferrihydrite-hematite recrystallization. *Geochim. Cosmochim. Acta* **206**, 236–253.

Bruggeman C., Maes A., Vancluysen J. and Vandemussele P. (2005) Selenite reduction in Boom clay: Effect of FeS_2, clay minerals and dissolved organic matter. *Environ. Pollut.* **137**, 209–21.

De Cannière P., Maes A., Williams S., Bruggeman C., Beauwens T., Maes N. and Cowper M. (2010) *Behaviour of Selenium in Boom Clay. External Report of the Belgian Nuclear Research Centre.*, SCK•CEN-ER-120, Mol, BEL.

Chakraborty S., Bardelli F. and Charlet L. (2010) Reactivities of Fe(II) on Calcite : Selenium Reduction. *Environ. Sci. Technol.* **44**, 1288–1294.

Charlet L., Scheinost A. C., Tournassat C., Greneche J. M., Géhin A., Fernández-Martínez A., Coudert S., Tisserand D. and Brendle J. (2007) Electron transfer at the mineral/water interface: Selenium reduction by ferrous iron sorbed on clay. *Geochim. Cosmochim. Acta* **71**, 5731–5749.

Chen Y.-W., Truong H.-Y. T. and Belzile N. (2009) Abiotic formation of elemental selenium and role of iron oxide surfaces. *Chemosphere* **74**, 1079–1084.

Cornell R. M. and Schwertmann U. (2003) *The iron oxydes: Structure, Properties, Reactions,* *Occurences and Uses*. 2nd ed., Wiley-VCH, Weinheim, Germany.

Curti E., Froideval-Zumbiehl A., Günther-Leopold I., Martin M., Bullemer A., Linder H., Borca C. N. and Grolimund D. (2014) Selenium redox speciation and coordination in high-burnup UO_2 fuel: Consequences for the release of ^{79}Se in a deep underground repository. *J. Nucl. Mater.* **453**, 98–106.

Curti E., Puranen A., Grolimund D., Jädernas D., Sheptyakov D. and Mesbah A. (2015) Characterization of selenium in UO_2 spent nuclear fuel by micro X-ray absorption spectroscopy and its thermodynamic stability. *Environ. Sci. Process. Impacts* **17**, 1760–1768.

Dhillon K. S. and Dhillon S. K. (2003) Distribution and management of seleniferous soils. *Adv. Agron.* **79**, 119–184.

Drissi H., Refait P. and Génin J.-M. R. (1994) The oxidation of $Fe(OH)_2$ in the presence of carbonate ions : Structure of carbonate green rust one. *Hyperfine Interact.* **90**, 395–400.

Fernández-Martínez A. and Charlet L. (2009) Selenium environmental cycling and bioavailability: A structural chemist point of view. *Rev. Environ. Sci. Biotechnol.* **8**, 81–110.

Génin J.-M. R., Ruby C., Géhin A. and Refait P. (2006) Synthesis of green rusts by oxidation of $Fe(OH)_2$, their products of oxidation and reduction of ferric oxyhydroxides; Eh-pH Pourbaix diagrams. *Comptes Rendus Geosci.* **338**, 433–446.

Grambow B. (2008) Mobile fission and activation products in nuclear waste disposal. *J. Contam. Hydrol.* **102**, 180–186.

Huber F., Schild D., Vitova T., Rothe J., Kirsch R. and Schäfer T. (2012) U(VI) removal kinetics in presence of synthetic magnetite nanoparticles. *Geochim. Cosmochim. Acta* **96**, 154–173.

Johnson T. M. and Bullen T. D. (2003) Selenium isotope fractionation during reduction by Fe(II)-Fe(III) hydroxide-sulfate (green rust). *Geochim. Cosmochim. Acta* **67**, 413–419.

Jordan N., Lomenech C., Marmier N., Giffaut E. and Ehrhardt J.-J. (2009) Sorption of selenium(IV) onto magnetite in the presence of silicic acid. *J. Colloid Interface Sci.* **329**, 17–23.

Jörg G., Bühnemann R., Hollas S., Kivel N., Kossert K., Van Winckel S. and Lierse v. Gostomski C. (2010) Preparation of radiochemically pure ^{79}Se and highly precise determination of its half-life. *Appl. Radiat. Isot.* **68**, 2339–2351.

Kämpf N., Scheinost A. C. and Schulze D. G. (2011) Oxide Minerals in Soils. In *Handbook of Soil Sciences: Properties and Processes* (eds. P. M. Huang, Y. Li, and M. E. Sumner). CRC Press, Boca Raton, USA. p. 1442.

Kang M., Ma B., Bardelli F., Chen F., Liu C., Zheng Z., Wu S. and Charlet L. (2013) Interaction of aqueous Se(IV)/Se(VI) with FeSe/$FeSe_2$: Implication to Se redox process. *J. Hazard. Mater.* **248–249**, 20–28.

Kurokawa H. and Senna M. (1999) Self-stabilization of green rust (II) as a precursor of acicular goethite particles with highest possible aspect ratio. *Powder Technol.*, 71–79.

Legrand L., Mazerolles L. and Chaussé A. (2004) The oxidation of carbonate green rust into ferric phases: Solid-state reaction or transformation via solution. *Geochim. Cosmochim. Acta* **68**, 3497–3507.

Lenz M. and Lens P. N. L. (2009) The essential toxin: The changing perception of selenium in environmental sciences. *Sci. Total Environ.* **407**, 3620–3633.

Liang L., Yang W., Guan X., Li J., Xu Z., Wu J., Huang Y. and Zhang X. (2013) Kinetics and mechanisms of pH-dependent selenite removal by zero valent iron. *Water Res.* **47**, 5846–5855.

Loyo R. L. de A., Nikitenko S. I., Scheinost A. C. and Simonoff M. (2008) Immobilization of selenite on Fe_3O_4 and Fe/Fe_3C ultrasmall particles. *Environ. Sci. Technol.* **42**, 2451–2456.

Miller W., Alexander R., Chapman N., McKinley J. C. and Smellie J. A. T. (2000) *Geological Disposal* *of Radioactive Wastes and Natural Analogues.*, Elsevier Science.

Missana T., Alonso U., Scheinost A. C., Granizo N. and García-Gutiérrez M. (2009) Selenite retention by nanocrystalline magnetite: Role of adsorption, reduction and dissolution/co-precipitation processes. *Geochim. Cosmochim. Acta* **73**, 6205–6217.

Mitchell K., Couture R.-M., Johnson T. M., Mason P. R. D. and Van Cappellen P. (2013) Selenium sorption and isotope fractionation: Iron(III) oxides versus iron(II) sulfides. *Chem. Geol.* **342**, 21–28.

Mullet M., Guillemin Y. and Ruby C. (2008) Oxidation and deprotonation of synthetic Fe^{II}-Fe^{III} (oxy)hydroxycarbonate Green Rust: An X-ray photoelectron study. *J. Solid State Chem.* **181**, 81–89.

Murphy A. P. (1988) Removal of selenate from water by chemical reduction. *Ind. Eng. Chem. Res.* **27**, 187–191.

Myneni S. C. B., Tokunaga T. K., Brown Jr., G. E. (1997) Abiotic Selenium Redox Transformations in the Presence of Fe(II,III) Oxides. *Science* . **278**, 1106–1109.

Nothstein A. K., Eiche E., Riemann M., Nick P., Winkel L. H. E., Göttlicher J., Steininger R., Brendel R., Von Brasch M., Konrad G. and Neumann T. (2016) Tracking Se Assimilation and Speciation through the Rice Plant - Nutrient Competition, Toxicity and Distribution. *PLoS One* **11**.

Olegario J. T., Yee N., Miller M., Sczepaniak J. and Manning B. (2010) Reduction of Se(VI) to Se(-II) by zerovalent iron nanoparticle suspensions. *J. Nanoparticle Res.* **12**, 2057–2068.

Perez O. P. and Umetsu Y. (2000) ORP-monitored magnetite formation from aqueous solutions at low temperatures. *Hydrometallurgy* **55**, 35–56.

Perez O. P., Umetsu Y. and Sasaki H. (1998) Precipitation and densification of magnetic iron compounds from aqueous solutions at room temperature. *Hydrometallurgy* **50**, 223–242.

Rebodos R. L. and Vikesland P. J. (2010) Effects of oxidation on the magnetization of nanoparticulate magnetite. *Langmuir* **26**, 16745–16753.

Refait P., Abdelmoula M. and Génin J.-M. R. (1998) Mechanisms of formation and structure of green rust one in aqueous corrosion of iron in the presence of chloride ions. *Corros. Sci.* **40**, 1547–1560.

Refait P., Simon L. and Génin J.-M. R. (2000) Reduction of SeO_4^{2-} Anions and Anoxic Formation of Iron (II) - Iron (III) Hydroxy-Selenate Green Rust. *Environ. Sci. Technol.* **34**, 819–825.

Ressler T. (1998) WinXAS: a program for X-ray absorption spectroscopy data analysis under MS-Windows. *J. Synchrotron Radiat.* **5**, 118–122.

Rossberg A., Reich T. and Bernhard G. (2003) Complexation of uranium(VI) with protocatechuic acid-application of iterative transformation factor analysis to EXAFS spectroscopy. *Anal. Bioanal. Chem.* **376**, 631–638.

Rovira M., Giménez J., Martínez M., Martínez-Lladó X., de Pablo J., Martí V. and Duro L. (2008) Sorption of selenium(IV) and selenium(VI) onto natural iron oxides: Goethite and hematite. *J. Hazard. Mater.* **150**, 279–284.

Scheidegger A. M., Grolimund D., Cui D., Devoy J., Spahiu K., Wersin P., Bonhoure I. and Janousch M. (2003) Reduction of selenite on iron surfaces: A microspectroscopic study. *J. Phys. IV* **104**, 417–420.

Scheinost A. C. and Charlet L. (2008) Selenite reduction by mackinawite, magnetite and siderite: XAS characterization of nanosized redox products. *Environ. Sci. Technol.* **42**, 1984–1989.

Scheinost A. C., Kirsch R., Banerjee D., Fernandez-Martinez A., Zaenker H., Funke H. and Charlet L. (2008) X-ray absorption and photoelectron spectroscopy investigation of selenite reduction by FeII-bearing minerals. *J. Contam. Hydrol.* **102**, 228–245.

Schwertmann U. and Cornell R. M. (2000) *Iron oxides in the laboratory: Preparation and* *characterization*. 2nd ed., Wiley-VCH, Weinheim, Germany.

Schwertmann U. and Fechter H. (1994) The formation of green rust and its transformation to lepidocrocite. *Clay Miner.* **29**, 87–92.

Séby F., Potin-Gautier M., Giffaut E., Borge G. and Donard O. F. X. (2001) A critical review of thermodynamic data for selenium species at 25°C. *Chem. Geol.* **171**, 173–194.

Séby F., Potin-Gautier M., Giffaut E. and Donard O. F. X. (1998) Review Assessing the speciation and the biogeochemical processes affecting the mobility of selenium from a geological repository of radioactive wastes to the biosphere. *Analusis* **26**, 193–198.

Smailos E., Schwarzkopf W., Kienzler B. and Köster R. (1992) Corrosion of carbon-steel container for heat-generating nuclear waste in brine environment relevant for a rock-salt repository. *MRS Proc.* **257**, 299–406.

Smart N. R., Rance A. P. and Werme L. O. (2008) The effect of radiation on the anaerobic corrosion of steel. *J. Nucl. Mater.* **379**, 97–104.

Sumoondur A., Shaw S., Ahmed I. and Benning L. G. (2008) Green rust as a precursor for magnetite: an in situ synchrotron based study. *Mineral. Mag.* **72**, 201–204.

Tang C., Huang Y. H., Zeng H. and Zhang Z. (2014) Reductive removal of selenate by zero-valent iron: The roles of aqueous Fe^{2+} and corrosion products, and selenate removal mechanisms. *Water Res.* **67**, 166–174.

Tang J., Myers M., Bosnick K. a and Brus L. E. (2003) Magnetite Fe_3O_4 Nanocrystals: Spectroscopic Observation of Aqueous Oxidation Kinetics. *J. Phys. Chem. B* **107**, 7501–7506.

Wang Y., Morin G., Ona-Nguema G., Juillot F., Calas G. and Brown G. E. (2011) Distinctive arsenic(V) trapping modes by magnetite nanoparticles induced by different sorption processes. *Environ. Sci. Technol.* **45**, 7258–7266.

Wersin P., Johnson L. H., Schwyn B., Berner U. and Curti E. (2003) *Redox Conditions in the Near Field of a Repository for SF/HLW and ILW in Opalinus Clay. NAGRA Technical Report 02-13.*, Wettingen, CH.

Winkel L. H. E., Vriens B., Jones G. D., Schneider L. S., Pilon-Smits E. and Bañuelos G. S. (2015) Selenium Cycling Across Soil-Plant-Atmosphere Interfaces: A Critical Review. *Nutrients* **7**, 4199–4239.

Yoon I.-H., Kim K.-W., Bang S. and Kim M. G. (2011) Reduction and adsorption mechanisms of selenate by zero-valent iron and related iron corrosion. *Appl. Catal. B Environ.* **104**, 185–192.

Zingaro R. A., Dufner D. C., Murphy A. P. and Moody C. D. (1997) Reduction of oxoselenium anions by iron(II) hydroxide. *Environ. Int.* **23**, 299–304.